Physica B 688 (2024) 416166

Contents lists available at ScienceDirect

Physica B: Condensed Matter

journal homepage: www.elsevier.com/locate/physb

Iridium's influence on the structural, electronic and mechanical characteristics of $ZrCo_{1-x}Ir_xSb$ half-heusler alloys

B. Abdelkebir [a,c], Z. Charifi [b,c,*], H. Baaziz [b,c], T. Ghellab [b,c], R. Khenata [a,**], S. Bin-Omran [d]

[a] Laboratoire de Physique Quantique de la Matière et de Modélisation Mathématique, Université de Mascara, 29000, Mascara, Algeria
[b] Department of Physics, Faculty of Science, University of M'sila, 28000, M'sila, Algeria
[c] Laboratory of Physics and Chemistry of Materials, University of M'sila, Algeria
[d] Department of Physics and Astronomy, College of Science, King Saud University, P.O. Box 2455, Riyadh, 11451, Saudi Arabia

ARTICLE INFO

Keywords:
Heusler alloys
Structural properties
Semiconductor
Elastic constants

ABSTRACT

Structural, electronic and mechanical *properties of* $ZrCo_{1-x}Ir_xSb$ *Half-Heusler alloys with varying x concentrations (x = 0, 0.125, 0.25, 0.375, 0.5, 0.625, 0.75, 0.875, and 1) were studied by performing the exchange-correlation (XC) energy evaluated using the local density (LDA) and generalized gradient (GGA) approximations. The calculated lattice constant, bulk modulus, and band gap energy of the ternary alloy show good agreement with previous theoretical predictions. The results indicate that an increase in Ir atom concentration in the alloy leads to an enlargement of the lattice constant (from 6.10 to 6.36 Å) and bulk modulus (from 138.09 to 149.*70 GPa*), resulting in increased volume and hardness of the compound. Moreover, the Engel-Vosko generalized gradient approximation (EVGGA) and modified Becke-Johnson (mBJ) schemes were employed to improve the calculations of the band structure and density of states. The studied alloys exhibit semiconductor characteristics, with a direct band gap for both x = 0.75 and x = 0.875 concentrations and an indirect band gap for the rest of the concentrations.* The computed elastic constants for $ZrCo_{1-x}Ir_xSb$ alloys satisfy the requirements for mechanical stability. The VRH approximations have been used to determine the bulk modulus, shear modulus, Young's modulus, Poisson's ratio and Hardness. In addition, we also determined the anisotropy factor, sound velocities and Debye temperature.

1. Introduction

Heusler alloys, named after Fritz Heusler, the German metallurgical engineer and chemist who discovered them in 1903 while he was studying the electrical conductivity of certain metallic alloys. He observed that an alloy composed of copper, manganese, and aluminum (Cu_2MnAl) displayed ferromagnetic properties, even though none of its constituent elements were magnetic on their own [1–18]. This unexpected behavior intrigued researchers and led to further exploration of this new class of materials.

Heusler alloys are an amazing group of materials, and there are thousands of them today. Our study focuses on a particular type called "Half-Heusler" alloys, not "Full-Heusler" alloys. The special thing about Half-Heusler alloys is that they have relatively high Curie temperatures [19–22] and their structure is similar to the zinc blende phase. This similarity allows for the possibility of integrating magnetic devices into semiconductor technologies.

The compounds known as half-Heusler (HH) alloys have a structure called MgAgAs [23]. XYZ, an HH alloy, has a structure that is similar to the structure of a full-Heusler alloy X_2YZ. In this structure, X and Y are transition metals, and Z is an element from group III, IV, or V on the periodic table. However, sometimes Y is replaced by a rare earth or alkaline earth metal element. Fig. 1 illustrates the displayed structure. This type of half-Heusler structure is characterized by three interpenetrating sub-lattices of a face-centered cubic arrangement, with each lattice occupied by atoms X, Y, and Z [24]. Wyckoff's notations are used to describe the locations of atoms, such as 4a (0, 0, 0), 4b (1/2, 1/2, 1/2), and 4c (1/4, 1/4, 1/4) [25–27]. In theory, there are three different possible atomic arrangements in this type of structure, as shown in Table 1.

Half-Heusler alloys are known for their ability to combine with various elements. This combination leads to a diverse set of physical properties. Heusler alloys are fascinating materials that exhibit a range of unique properties, including ferromagnetism, shape memory, and

---

* Corresponding author.
** Corresponding author.
E-mail addresses: zoulikha@gmail.com, zoulikha.charifi@univ-msila.dz (Z. Charifi), rabah_khenata@univ-mascara.dz, khenata_rabah@yahoo.fr (R. Khenata).

https://doi.org/10.1016/j.physb.2024.416166
Received 26 October 2023; Received in revised form 26 May 2024; Accepted 31 May 2024

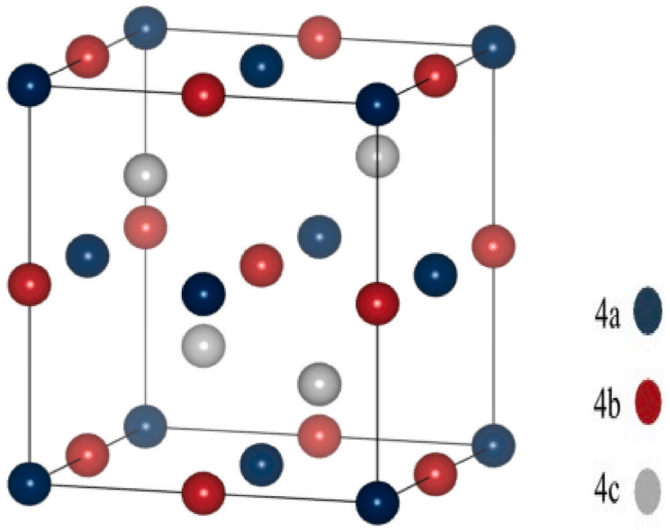

Fig. 1. The $C1_b$ structure (the half-Heusler alloy). Notations of atom positions: 4a (0,0,0), 4b (1/2,1/2,1/2) and 4c (1/4,1/4,1/4).

Table 1
The three equivalent site occupancy arrangements within the $C1_b$ type structure. Atoms in Wyckoff-type position.

	4a (0,0,0)	4b (0.5,0.5,0.5)	4c (0.25,0.25,0.25)
I	X	Y	Z
II	Z	X	Y
III	Y	Z	X

high thermoelectric efficiency. For example, the compound RbSrSi exhibits interesting electronic properties [28], TiCoSb shows thermoelectric properties [29], and NiMnSb displays magnetic characteristics as a half-metallic ferromagnet [30].

Half-Heusler alloys have several useful properties such as wide temperature stability [31,32], adjustable band gaps [33,34], and flexible composition. They find applications in various fields including topological insulators, spintronic devices [31], magnets, photovoltaics [34], optoelectronic devices [31,35], and thermoelectric applications [32–34] due to their high performance. These alloys have attracted the attention of many researchers [36] who have studied their band structures and properties. For example, Zahedifar et al. discovered that the energy gaps of half-Heusler alloys based on Sb range from 1.13 to 1.44 eV [37]. Additionally, p-type doping, $Zr_{0.5}Hf_{0.5}NiSn$ as reported by Zou et al. [38], improves the thermoelectric performance. In quaternary Heusler alloys (LiMgXSb), Nag et al.'s [39] studies showed that doping charge carriers within the unit cell can greatly increase ZT and power factor. The mechanical research by Kalita et al. [40] revealed that the ductility of the RuMnAs compound, ionic bonding, hardness of the material, and independent elastic constants (C_{11} and C_{12}) increase practically linearly with applied pressure. Chibani et al. [41] conducted an ab initio prediction on the structural, electronic, and elastic properties of half-Heusler ternary compounds TiIrX (X = As and Sb). Gupta and coworkers [42] studied the lattice dynamics of MnY_2Ga Full Heusler alloy in its the cubic phase ($L2_1$) and show that phonon vibrations are highly dependent on the surrounding spin and pressure. Besides contributing to their theoretical studies on the behavior of the novel AlNiX (X = As and Sb) half-Heusler alloys from a thermoelectric standpoint, both alloys exhibit n-type behavior, as indicated by their negative Seebeck coefficient [43]. They clarified that increasing the Seebeck coefficient might be substituted with the appropriate doping substituent or nano-structuring procedures. Increasing its thermoelectric performance as a result [44]. Furthermore, Gupta and coauthors anticipated that AlNiAs are more ductile than AlNiSb from a mechanical perspective [45].

In this paper, we focus on studying the structural, electronic and mechanical properties of $ZrCo_{1-x}Ir_xSb$ half-Heusler alloys. These alloys have different compositions, ranging from x = 0 to 1, and possess a cubic MgAgAs-type structure with 18 valence electrons. To analyze these properties, we employ first-principles calculations based on density functional theory (DFT) [46,47]. The electronic analysis reveals that both ternary compounds exhibit semiconductor characteristics with a wide band gap. The paper is organized into three main sections: computational methods, results and discussion, and conclusion. In the computational methods section, we provide a concise explanation of our computational approach. In the results and discussion section, our findings on the optimized lattice constant, electronic and mechanical properties of the half-Heusler alloys are presented. Finally, the conclusion section summarizes our study's key findings

2. Computational methods

In our computational work, we utilized the Full Potential Linearized Augmented Plane Wave method (FP-LAPW) [48,49] in conjunction with Density Functional Theory (DFT) [46,47], as implemented through the WIEN-2K software [50]. This approach allows us to investigate the electronic structure of crystals. To simplify the representation of the crystal's potential, the "muffin-tin approximation" was applied, which divides the system into two distinct regions. In the first region corresponds to atomic spheres centered on atomic sites, the radial solutions of the Schrödinger equation were employed. The second region encompasses the remaining interstitial space and is analyzed using a plane wave expansion [51]. To determine the structural properties of the alloys under considirations, two fundamental densities functional theory (DFT) approximations were performed: The Local Density Approximation (LDA) [52] and the Generalized Gradient Approximation developed by Perdew et al. (GGA-PBE) [53]. These approaches are used for estimating the exchange and correlation interactions. Recognizing that GGA and LDA often tend to underestimate the band gap, we adopted two complementary methods to improve gap calculations. Firstly, the Engel-Vosko's GGA correction formula (EV-GGA) was incorporated [54], which has shown significant improvements in predicting band gaps, particularly for compounds of interest. Additionally, the modified Becke–Johnson (mBJ) [55] approach was integrated into our calculations. The mBJ formalism is known for accurately describing semiconductor band gaps and offering a more precise representation of the electronic band structure. To ensure the structural stability of the herein studied alloys, atomic position relaxation was performed by minimizing external forces acting on the atoms. This relaxation process was carried out with the support of both the GGA and LDA approximations, contributing to a reliable structural analysis.

To achieve the desired alloy compositions represented by x values of 0.25, 0.75 and 1, we implemented a substitution strategy. Specifically, one, three and four cobalt (Co) cation sites were replaced with iridium (Ir) atoms within a unit cell containing four atoms. Conversely, to obtain alloys with x values of 0.125, 0.375, 0.5, 0.625, and 0.875, we introduced substitutions on one, three, four, five, and seven Co cation sites, respectively, using Ir atoms in an expanded supercell consisting of eight atoms. In this process, the valence states of Zr ([Kr] 4 d^2 $5s^2$), Co ([Ar] 3 d^7 $4s^2$), Ir ([Xe] $4f^{14}$ 5 d^7 $6s^2$), and Sb ([Kr] 4 d^{10} $5s^2$ $5p^3$) were considered for our predictions. Additionally, the remaining states as core states within the electronic configuration of each material were treated.

In order to ascertain the structural and electronic attributes of the compounds under investigation, a high-density k-point mesh, consisting of 800 k-points within the Brillouin zone (BZ), was emeployed during our total energy calculations. The expansion of the wave function in the interstitial region for all nine HH alloys was conducted with a plane wave cutoff $R_{M.T}K_{\max} = 8$. In our computations, the Muffin-Tin Radius

Table 2
Different atomic combinations in the ZrXSb (X = Co and Ir) half-Heusler structure.

The compounds	Atoms	arrangement 1 (4c, 4a, 4b)	arrangement 2 (4a, 4b, 4c)	arrangement 3 (4b, 4c, 4a)
ZrXSb	***Zr***	(0.25,0.25,0.25)	(0,0,0)	(0.5,0.5,0.5)
	X	(0,0,0)	(0.5,0.5,0.5)	(0.25,0.25,0.25)
	Sb	(0.5,0.5,0.5)	(0.25,0.25,0.25)	(0,0,0)

exhibited variations spanning from 2.33 to 2.5 atomic units. To ensure the convergence of energy to an approximate tolerance of 10-^{5} Ry, iterative self-consistent iterations were iteratively conducted. To obtain the ground state parameters, the total energy dependence of the cell volume is fitted to the Birch-Murnaghan equations of state [56,57], which is seen in Equation (1).

$$E(V)=E_0+\frac{9V_0B_0}{16}\left\{\left[\left(\frac{V_0}{V}\right)^{\frac{2}{3}}-1\right]^3B_0'+\left[\left(\frac{V_0}{V}\right)^{\frac{2}{3}}-1\right]^2\left[6-4\left(\frac{V_0}{V}\right)^{\frac{2}{3}}\right]\right\} \qquad (1)$$

Where E_0 is the least amount of energy at T = 0 K, B is the bulk modulus, B' is the bulk modulus derivative and V_0 is the equivalent amount of volume.

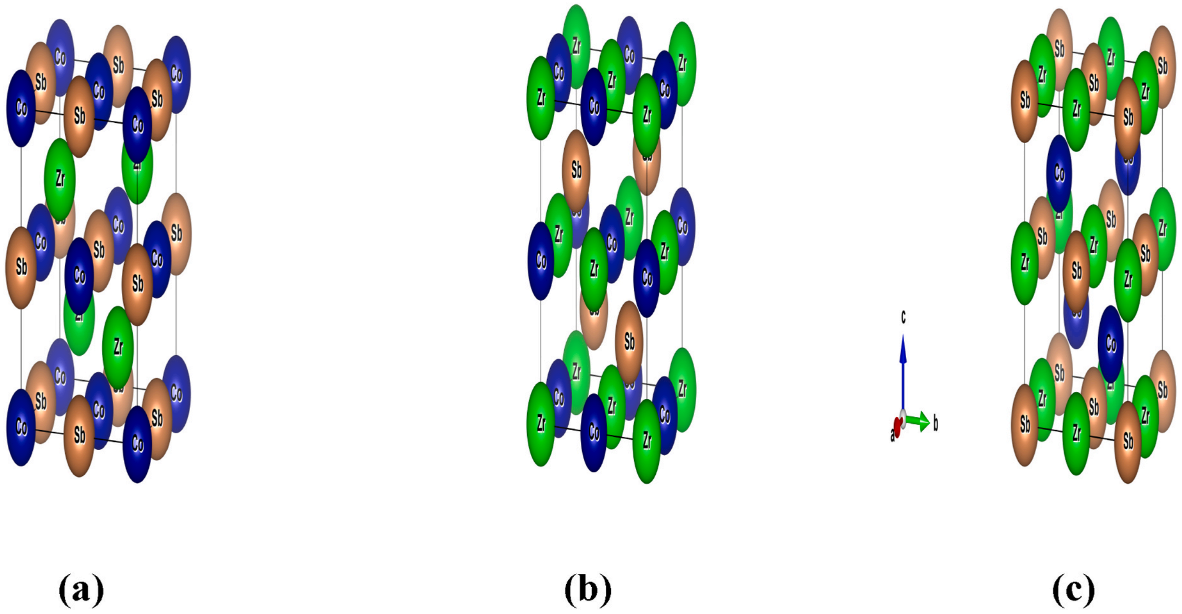

(a) **(b)** **(c)**

Fig. 2. ZrCoSb HH alloy crystal structure in (a) arrangement 1, (b) arrangement 2, and (c) arrangement 3.

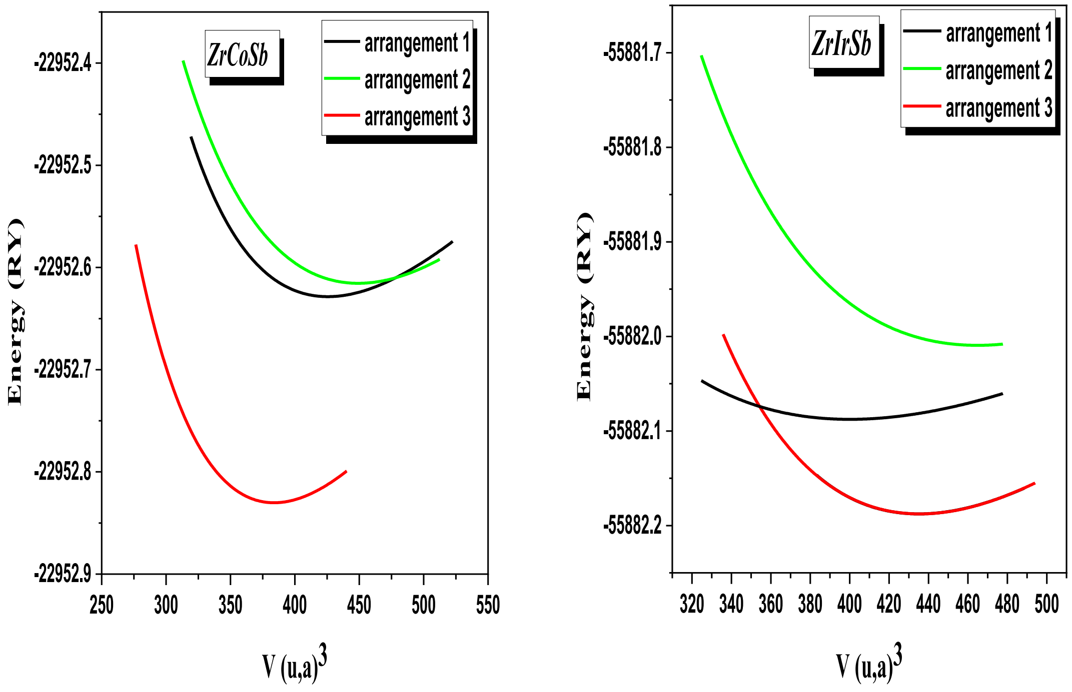

Fig. 3. The energy variation as a function of volume for ZrCoSb and ZrIrSb compounds in arrangements 1, 2, and 3.

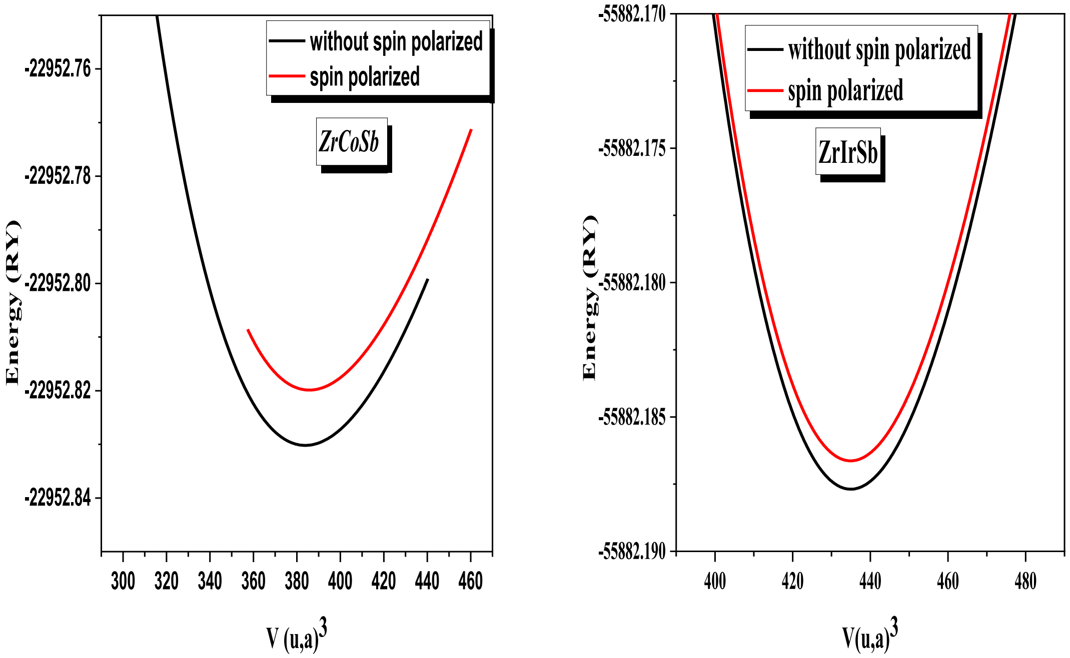

Fig. 4. The variation of the energy as a function of the volume for ZrCoSb and ZrIrSb compounds in the states of polarized spin (FM state) and without polarized spin (NM state).

3. Results and discussion

3.1. Structural properties

Under ambient conditions, it is notable that ZrXSb alloys, where X stands for either cobalt (Co) or iridium (Ir), adopt a specific crystalline arrangement referred to as a face-centered cubic (FCC) structure. This FCC structure is categorized under the space group No. 216, $F\bar{4}3m$ which describes the arrangement of atoms in the crystal lattice. It is important to mention that within the framework of the half-Heusler (HH) structure, there are three distinct atomic configurations, each characterized by unique spatial arrangements of atoms. It's noteworthy that within the half-Heusler (HH) structure, there exist three unique atomic configurations, each with distinct atom arrangements. To proceed with our research and conduct accurate calculations, it is crucial to determine which of these atomic configurations is the most stable. This essential determination, as detailed in Table 2 and illustrated in Fig. 2, serves as the foundational step in our computational analyses. The choice of the most stable configuration significantly influences the subsequent stages of the present investigation, enabling us to gain deeper insights into the properties and behaviors of these materials.

In the present investigation of ZrCoSb and ZrIrSb alloys, three distinct atomic arrangements denoted as 1, 2, and 3 were considered, the total energy were systematically calculated while varying the volume. The results of these comprehensive calculations are thoughtfully presented in Fig. 3. Upon careful examination of the data presented in Fig. 3, a clear and compelling conclusion emerges: the atomic configuration characterized by the arrangement 3 structure (4b, 4c, 4a) stands out as the most stable among the options considered. This structural arrangement exhibits the lowest total energy across the range of volumes investigated, signifying its preference in terms of stability within the context of our study.

In this investigation of ZrXSb compounds, where X represents either cobalt (Co) or iridium (Ir), a rigorous analysis of total energies within two distinct spin states have conducted: the polarized spin state (Ferromagnetic or FM State) and the non-polarized spin state (Non-Magnetic or NM State). These calculations were performed specifically within the framework of the arrangement 3 structure, denoted as (4b, 4c, 4a). The compelling insights drawn from our computational results, as visually represented in Fig. 4, reveal a consistent and significant trend. Notably, it becomes evident that the lowest energy state is consistently associated with the non-polarized spin configuration (NM State) within the arrangement 3 structure (4b, 4c, 4a) for both ZrCoSb and ZrIrSb compounds. This outcome underscores the remarkable stability of this particular structural configuration, characterized by the absence of spin polarization, within the context of our investigation into ZrXSb (X = Co and Ir) compounds.

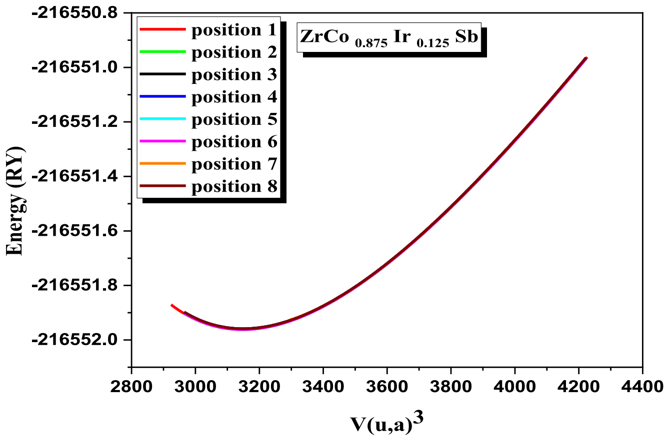

Fig. 5. The variation of the energy as a function of the volume in the Ir-doped states at eight different Co positions.

As mentioned in the Computational Methods section, our approach involved the substitution of one cobalt (Co) cation site with iridium (Ir) atoms within an eight-atom supercell to create the alloy with a concentration of x = 0.125. It is worth noting that the structural integrity and the accuracy of our calculations remained unaffected by the substitution of an Ir atom for one of the eight Co atoms in various positions (see Fig. 5). This observation holds true consistently across all the alloys examined.

In Fig. 6, we present a graphical representation of the half-Heusler

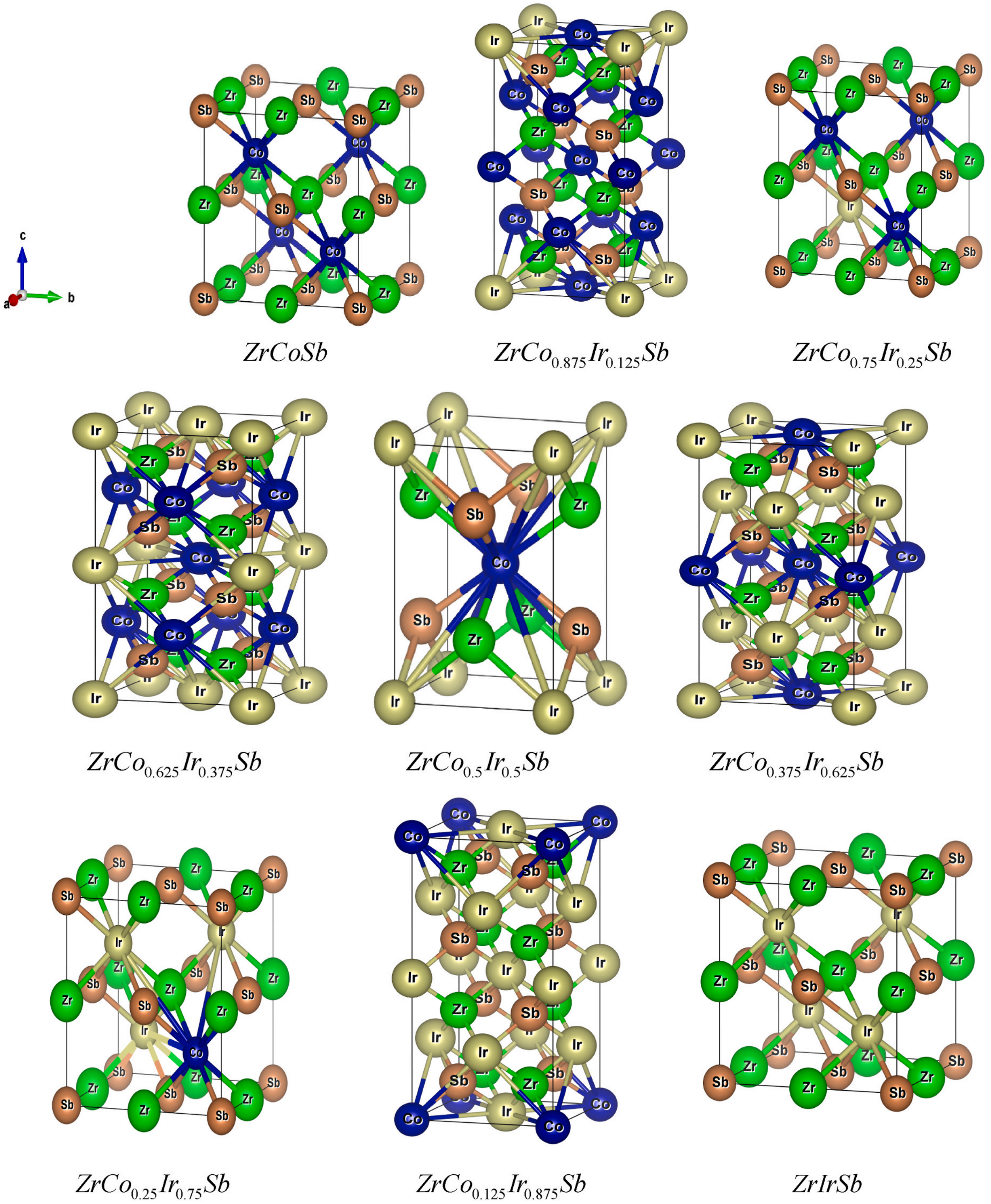

$ZrCoSb$ $ZrCo_{0.875}Ir_{0.125}Sb$ $ZrCo_{0.75}Ir_{0.25}Sb$

$ZrCo_{0.625}Ir_{0.375}Sb$ $ZrCo_{0.5}Ir_{0.5}Sb$ $ZrCo_{0.375}Ir_{0.625}Sb$

$ZrCo_{0.25}Ir_{0.75}Sb$ $ZrCo_{0.125}Ir_{0.875}Sb$ $ZrIrSb$

Fig. 6. $ZrCo_{1-x}Ir_xSb$ (x = 0, 0.125, 0.25, 0.375, 0.5, 0.625, 0.75, 0.875 and 1) half-Heusler alloy crystal structures.

structures $ZrCo_{1-x}Ir_xSb$ for varying concentrations (x = 0, 0.125, 0.25, 0.375, 0.5, 0.625, 0.75, 0.875, and 1). Additionally, Table 3 provides a detailed account of the atomic positions within these structures, considering both the Generalized Gradient Approximation (GGA) and the Local Density Approximation (LDA). These comprehensive visual and tabular representations serve as valuable resources for our analysis and offer insights into the structural variations across the different alloy compositions.

In our present study, the Brich-Murnaghan equation of state [56,57] presented in equation (1) was employed. This equation was utilized to model the relationship between total energy and volume, enabling us to explore structural characteristics, including lattice constants (a) and the bulk modulus (B), across a range of concentrations (x = 0, 0.125, 0.25, 0.375, 0.5, 0.625, 0.75, 0.875, and 1) in $ZrCo_{1-x}Ir_xSb$ half-Heusler alloys. Table 4 displays our predictions for ternary semiconductors and their mixtures. We're comparing these predictions to measurements of the lattice constant. It's important to note that when LDA calculations was used, the lattice constants turn out to be smaller than what theory suggests, but with GGA, they tend to be larger. Interestingly, for ZrCoSb and ZrIrSb ternary compounds, our GGA results match up really well with what previous research and experiments have found. Fig. 7 (a) represents the variation of the equilibrium lattice parameter as we vary

Table 3
Calculated atomic positions (fractional coordinates) of the alloy $ZrCo_{1-x}Ir_xSb$ (x = 0, 0.125, 0.25, 0.375, 0.5, 0.625, 0.75, 0.875 and 1) with the GGA and LDA approximations.

The compounds	GGA	LDA
$ZrCoSb$ 216_$F-\bar{4}3m$	***Zr***: 0.5, 0.5, 0.5 ***Co***: 0.25, 0.25, 0.25 ***Sb***: 0, 0, 0	***Zr***: 0.5, 0.5, 0.5 ***Co***: 0.25, 0.25, 0.25 ***Sb***: 0, 0, 0
$ZrCo_{0.875}Ir_{0.125}Sb$ 111_$P-\bar{4}2m$	***Zr***: 0.7455, 0.7455, 0.8711 ***Co***: 05, 0, 02524 ***Ir***: 0, 0, 0 ***Sb***: 02546, 07453, 0.8714	***Zr***: 02519, 07480, 08735 ***Co***: 0.5, 0, 02503 ***Ir***: 0, 0, 0 ***Sb***: 0.4757, 0.4757, 0.8726
$ZrCo_{0.75}Ir_{0.25}Sb$ 215_$P-\bar{4}3m$	***Zr***: 0.2532, 0. 2532, 0. 2532 ***Co***: 0.5, 0.5, 0 ***Ir***: 0, 0, 0 ***Sb***: 0.7457, 0.7457, 0.7457	***Zr***: 0.0016, 0.9983, 0.9983 ***Co***: 0.25, 0.75, 0.25 ***Ir***: 0.75, 0.25, 0.25 ***Sb***: 0.4952, 0.9952, 0.9952
$ZrCo_{0.625}Ir_{0.375}Sb$ 111_$P-\bar{4}2m$	***Zr***: 0.2501, 0.7498, 0.8722. ***Co***: 0.5, 0, 0.2510 ***Ir***: 0, 0, 0 ***Sb***: 0.7501, 0.7501, 0.8694	***Zr***: 0.2501, 0.7498, 0.8725 ***Co***: 0.5, 0, 0.2509 ***Ir***: 0, 0, 0 ***Sb***: 0.7501, 0.7501, 0.8693
$ZrCo_{0.5}Ir_{0.5}Sb$ 115_$P-\bar{4}m2$	***Zr***: 0.4999, 0.4999, 0.9966 ***Co***: 0.25, 0.25, 0.75 ***Ir***: 0.25, 0.75, 0.25 ***Sb***: 0.4999, 0.499, 0.5100	***Zr***: 0.5, 0.4999, 0.9973 ***Co***: 0.75, 0.75, 0.75 ***Ir***: 0.25, 0.75, 0.2499 ***Sb***: 0.9999, 0.4999, 0.9894
$ZrCo_{0.375}Ir_{0.625}Sb$ 111_$P-\bar{4}2m$	***Zr***: 0.7494, 0.7487, 0.1252 ***Co***: 0, 0, 0.5 ***Ir***: 0.5, 0, 0.4786 ***Sb***: 0.2499, 0.7500, 0.6193	***Zr***: 0.7499, 0.7499, 0.626 ***Co***: 0, 0, 0.5 ***Ir***: 0.5, 0, 0.7488 ***Sb***: 0.2499, 0.7500, 0.6194
$ZrCo_{0.25}Ir_{0.75}Sb$ 215_$P-\bar{4}3m$	***Zr***: 0.2459, 0.7540, 0.7540 ***Co***: 0, 0, 0 ***Ir***: 0, 0. 5, 0. 5 ***Sb***: 0.7548, 0.2451, 0.2451	***Zr***: 0.2479, 0.2479, 0.2479 ***Co***: 0, 0, 0 ***Ir***: 0, 0.5, 0 ***Sb***: 0.7551, 0.2448, 0.2448
$ZrCo_{0.125}Ir_{0.875}Sb$ 111_$P-\bar{4}2m$	***Zr***: 0.2478 0.7521, 0.8769 ***Co***: 0, 0, 0 ***Ir***: 0.5, 0, 0.2487 ***Sb***: 0.7551, 0.7551, 0.8780	***Zr***: 0.7481, 0.7481, 0.6231 ***Co***: 0, 0.5, 0.5 ***Ir***: 0.5, 0, 0.7486 ***Sb***: 0.2556, 0.7443, 0.6217
$ZrIrSb$ 216_$F-\bar{4}3m$	***Zr***: 0.5, 0.5, 0.5 ***Ir***: 0.25, 0.25, 0.25 ***Sb***: 0, 0, 0	***Zr***: 0.5, 0.5, 0.5 ***Ir***: 0.25, 0.25, 0.25 ***Sb***: 0, 0, 0

the composition of the alloys. Interestingly, it's evident that there is a slight deviation from Vegard's law [58], with a noticeable downward curvature measuring 0.2576 Å.

Our results for the lattice constants of ternary semiconductors ZrCoSb and ZrIrSb exhibit excellent agreement with experimental data [59,60,63] and concur with theoretical predictions found in previous references [61,62]. Furthermore, a noteworthy observation pertains to the influence of increasing Ir concentration (x = 0, 0.125, 0.25, 0.375, 0.5, 0.625, 0.75, 0.875, and 1) on the lattice constant. We observed a progressive expansion in the lattice as the Ir content increased (x = 0, 0.125, 0.25, 0.375, 0.5, 0.625, 0.75, 0.875, and 1). This behavior can be attributed to the comparatively larger atomic radius of Ir (r = 2.02) relative to Co (r = 1.92). Consequently, the introduction of Ir into the lattice led to its expansion, a phenomenon that our study duly captured and substantiated.

In Fig. 7 (b), we present also the bulk modulus of the $ZrCo_{1-x}Ir_xSb$ alloy as a function of composition (x = 0, 0.125, 0.25, 0.375, 0.5, 0.625, 0.75, 0.875, and 1). Notably, the observed behavior of the bulk modulus deviates from a linear concentration dependence, demonstrating a concave curve with a distinct downward curvature measuring 12.6632 GPa. Furthermore, our investigation reveals a noteworthy relationship between the bulk modulus and the concentration of Ir within $ZrCo_{1-x}Ir_xSb$ half-Heusler alloy. As the concentration of Ir increased, a corresponding increase in the alloy's hardness was observed, suggesting a direct influence of Ir content on the mechanical properties of the material. We've noticed that there are no existing theoretical or experimental structural parameter data for alloys with x values of 0.125, 0.25, 0.375, 0.5, 0.625, 0.75, and 0.875. This means we don't have any prior data to compare our results to.

3.2. *Electronic properties*

Careful adjustment of a material's band structure, achieved through methods like doping, alloying, or strain engineering, plays a crucial role in customizing materials for specific purposes. This customization can lead to the creation of better semiconductor devices, more efficient solar cells, and innovative electronic states. Consequently, understanding and managing band structures are central to progress in a wide range of scientific and technological fields.

We conducted band structure calculations for $ZrCo_{1-x}Ir_xSb$ half-Heusler compounds with different compositions, ranging from x = 0 to x = 1, by performing various approximations, namely GGA, LDA, EV-GGA, and mBJ-GGA. In the resulting figures (Fig. 8(a)-(k)), one can observe that the ternary compounds ZrIrSb (ZrCoSb) show indirect band gaps occurred between specific points in the Brillouin Zone, specifically between the L point for ZrCoSb and Γ for ZrIrSb and the X point. The X point marks the minimum energy level of the conduction band (CBM) within the first Brillouin Zone. This phenomenon of having indirect band gaps is not unique to these compounds but has been observed in other well-known semiconducting half-Heusler materials, such as ZrNiSn and HfNiSn [64].

In the analysis of the band structures for the compounds $ZrCo_{0.25}Ir_{0.75}Sb$ and $ZrCo_{0.125}Ir_{0.875}Sb$ represented in Fig. 8(g) and (h), distinctive characteristics emerge. These compounds exhibit substantial "large direct gaps" within their electronic structures, a notable phenomenon wherein the conduction band minimum (CBM) aligns precisely with the valence band maximum (VBM) at the same point Γ within the first Brillouin Zone.

Conversely, in the band structure diagrams for alloys characterized by x values of 0.125, 0.375, and 0.625, as illustrated in Fig. 8(b), (d), and 8(f), a distinct presence of "indirect band gaps" M-Γ becomes evident. In these scenarios, the VBM and CBM do not coexist at the same point within the Brillouin Zone, necessitating alterations in both energy and momentum during electronic transitions. Furthermore, in Fig. 8(e) and (c), we also observe indirect band gaps, but with the VBM located at specific midpoints, (Γ, X or R), while the CBM resides at a different position Γ. These findings underscore the indirect nature of these band gaps. Consequently, our comprehensive analysis of all half-Heusler alloys encompassing x values ranging from 0 to 1 consistently reveals their semiconductor nature. In Table 5, our calculated band gap values for the entire set of half-Heusler alloys are summarized. A noticeable trend emerges from our analysis: the indirect band gaps are consistently smaller in magnitude when compared to the values of the direct band gaps. This means that, for the majority of the alloys in our investigation, electron transitions requiring a change in both energy and momentum (indirect transitions) are associated with smaller energy gaps. However, it's worth noting that an exception to this pattern is observed in the case of the ZrIrSb alloy, where the indirect band gap exhibits a different behavior.

it is widely acknowledged that GGA and LDA tend to underestimate band gaps to some degree. To address the limitations of GGA and LDA and enhance the accuracy of our band structure calculations, the EV-GGA and mBJ-GGA (modified Becke-Johnson GGA) methods were adopted. These advanced techniques are designed to maximize the

Table 4

Calculated lattice parameter $a(A^{\circ})$ bulk modulus $B(GPa)$, minimum energy $E_{\min}(Ry)$ and volume $(Bohr)^3$ for ZrCo$_{1-x}$Ir$_x$Sb (x = 0, 0.125, 0.25, 0.375, 0.5, 0.625, 0.75, 0.875 and 1) compounds, as well as additional theoretical and experimental results.

The compounds	The parameters	This work (GGA)	This work (LDA)	Others
ZrCoSb 216_$F-\bar{4}3m$	***a (Å)***	6.1039	5.9809	6.068 [59] 6.070 [60] 6.094 [61]
	B (GPa)	138.0990	162.1507	-
	V_0 (Bohr) ^{3}	383.6680	360.9413	-
	E_{min} (Ry)	−22952.834551	−22929.465912	-
ZrCo$_{0.875}$Ir$_{0.125}$Sb 111_$P-\bar{4}2m$	***a (Å)***	6,14	6.0310	-
	B (GPa)	139.0244	164.4817	-
	V_0 (Bohr) ^{3}	3124.9454	2960.7253	-
	E_{min} (Ry)	−216551.972206	−216349.609087	-
ZrCo$_{0.75}$Ir$_{0.25}$Sb 215_$P-\bar{4}3m$	***a (Å)***	6.1799	6.0690	-
	B (GPa)	140.0679	165.1681	-
	V_0 (Bohr) ^{3}	1592.7230	1508.5092	-
	E_{min} (Ry)	−124740.662143	−124631.747409	-
ZrCo$_{0.625}$Ir$_{0.375}$Sb 111_$P-\bar{4}2m$	***a (Å)***	6.218	6.1044	-
	B (GPa)	143.2527	166.3228	-
	V_0 (Bohr) ^{3}	3246.2788	3070.2110	-
	E_{min} (Ry)	−282410.683545	−282177.386230	-
ZrCo$_{0.5}$Ir$_{0.5}$Sb 115_$P-\bar{4}m2$	***a (Å)***	6.2505	6.1391	-
	B (GPa)	144.1186	168.3162	-
	V_0 (Bohr) ^{3}	1647.9086	1561.4137	-
	E_{min} (Ry)	−157670.019168	−157545.637479	-
ZrCo$_{0.375}$Ir$_{0.625}$Sb 111_$P-\bar{4}2m$	***a (Å)***	6.282	6.1710	-
	B (GPa)	145.3984	169.6056	-
	V_0 (Bohr) ^{3}	3346.3314	3171.8610	-
	E_{min} (Ry)	−348269.397311	−348005.173204	-
ZrCo$_{0.25}$Ir$_{0.75}$Sb 215_$P-\bar{4}3m$	***a (Å)***	6.3058	6.2013	-
	B (GPa)	147.9010	171.3103	-
	V_0 (Bohr) ^{3}	1692.1051	1609.3532	-
	E_{min} (Ry)	−190599.378128	−190459.541904	-
ZrCo$_{0.125}$Ir$_{0.875}$Sb 111_$P-\bar{4}2m$	***a (Å)***	6,33	6.2313	-
	B (GPa)	149.2749	172.6333	-
	V_0 (Bohr) ^{3}	3438.5163	3265.7871	-
	E_{min} (Ry)	−414128.125943	−413832.988216	-
ZrIrSb 216_$F-\bar{4}3m$	***a (Å)***	6.3637	6.2581	6.358 [61] 6.370 [62] 6.292 [63]
	B (GPa)	149.7017	172.5638	-
	V_0 (Bohr) ^{3}	434.7671	413.4818	-
	E_{min} (Ry)	−55882.185573	−55843.362315	-

potential for precise band structure computations. The use of EV-GGA and mBJ-GGA is particularly advantageous because it leads to improved band separation and other electronic properties. The efficacy of these methods largely hinges on their ability to enhance the precision of the exchange-correlation potential, a pivotal component in density functional theory calculations. By implementing EV-GGA and mBJ-GGA, we aim to provide more accurate insights into the band structures of the materials under investigation, enabling a deeper understanding of their electronic behavior and paving the way for more informed materials design and engineering.

Analyzing the data in Table 5, one can see that the EV-GGA method tends to give us larger energy gap values compared to the mBJ-GGA method. In simpler terms, when EV-GGA is used, it often predicts that our materials have wider gaps between their energy levels.

Fig. 9 visually shows how the band gap (Eg) of ZrCo$_{1-x}$Ir$_x$Sb changes as increasing the amount of Ir in the alloys, going from 0.25 to 0.875. It is also reveals that as adding more Ir to the alloy, the band gap of the material gets bigger. This finding is important because it suggests that by carefully controlling the amount of Ir into the alloy, one can get materials with improved electronic properties, which could be useful for various applications.

Moreover, we conducted calculations of the total and partial densities of states (TDOS and PDOS) for ZrCo$_{1-x}$Ir$_x$Sb (x = 0, 0.125, 0.25, 0.375, 0.5, 0.625, 0.75, 0.875 and 1) half-Heusler alloys. These calculations were carried out using the EV-GGA approximations, aiming to provide a more comprehensive insight into the electronic structure of these materials. Our analysis of state densities revealed the presence of an energy gap near the Fermi level for all nine half-Heusler alloys under investigation. This significant finding is visually represented in Fig. 10 (a) to 10(k), where the energy gap manifests itself within the electronic structure of each alloy.

The ZrCoSb alloy exhibits a unique electronic structure characterized by three distinct valence band peaks. In the energy range from the Fermi level to approximately - 4 eV, these peaks are primarily influenced by the presence of Co − d states. Furthermore, within the energy range of −3 to −0.34 eV, Zr − d and Sb − p states also make a significant contribution to the valence band. Notably, these same atoms play a role in the conduction band, but with less prominence.

In the case of ZrIrSb, a similar pattern emerges with three discernible valence bands. However, the electronic states in the valence band between - 4 eV and roughly - 0.67 eV are predominantly governed by Ir − d states. Zr − d and Sb − p states make a comparatively smaller contribution in the energy range of −4 to −0.43 eV. Notably, the conduction band of the ZrIrSb compound is mainly formed by Zr − d states, with minimal input from Ir − d and Sb − p states.

The examination of the partial anticipated density of states (DOS) for ZrCo$_{1\text{-}x}$Ir$_x$Sb compounds, where x represents the concentrations of 0.125, 0.25, and 0.5, demonstrates the presence of three discernible peaks in the valence band. The dominant contribution to the highest valence band (VB) arises from the well-separated d states of the Co and Ir atoms. Conversely, the second peak mostly originates from the Ir-d state, with minor contributions from the Co-d and Sb-p states. The lowest valence band is mostly determined by a combination of atom contributions. The conduction bands (CB) are primarily governed by the Zr-

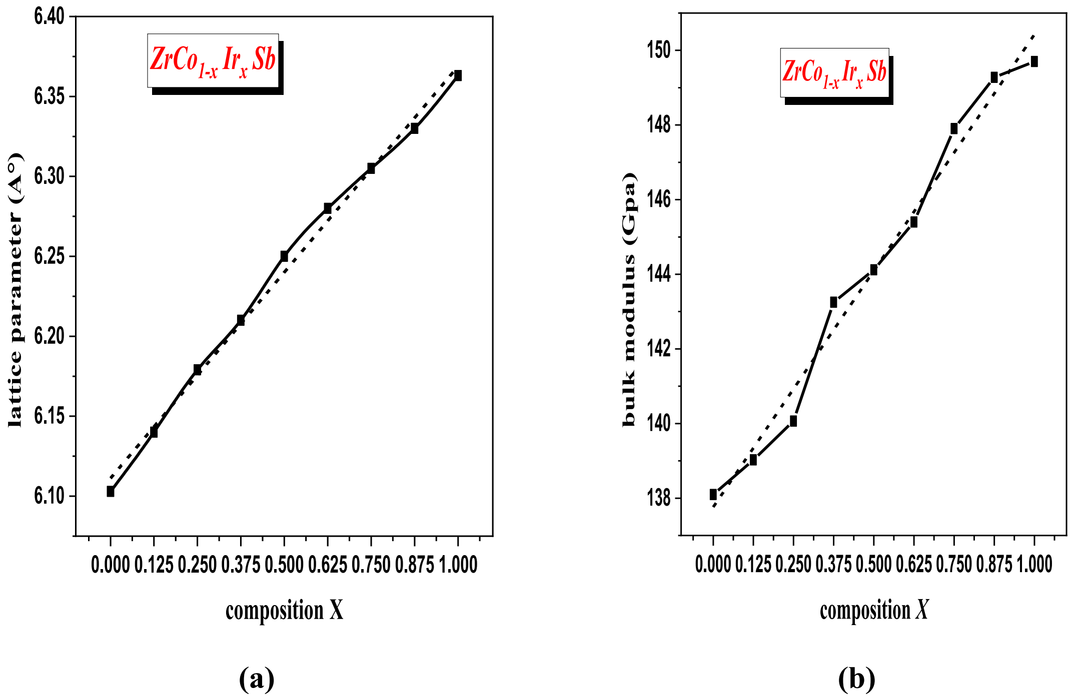

(a) (b)

Fig. 7. Composition dependence of the calculated (a) lattice constant and (b) bulk modulus (filled squares) of $ZrCo_{1-x}Ir_xSb$ alloy compared with the linear composition dependence prediction (dotted line).

d state, whereas the Co-d and Ir-d states make comparatively lesser contributions.

The density of states (DOS) analysis of ZrCo1-xIrxSb alloys (with x values of 0.375, 0.625, and 0.75) reveals that the Co-d and Ir-d states are the primary contributors to the overall DOS in the valence band (VB) region, particularly in the vicinity of the Fermi level. Notably, the Co-d state exhibits a somewhat higher contribution compared to the Ir-d state. In the (CB) area, our observations reveal a predominant presence of a hybridized combination of Zr-d and Co-d orbitals, with Zr-d orbitals making the principal contribution.

The final alloy investigated in the study, $ZrCo_{0.125}Ir_{0.875}Sb$, reveals the presence of two distinct zones inside the valence band (VB). Within the energy range of 5 to 3 electron volts (eV), the initial area predominantly consists of states attributed to iridium-d orbitals, accompanied by a minor contribution from zirconium-d and antimony-p orbitals. The Co-d orbitals are responsible for the formation of the second energy area, which spans from 3 eV to the Fermi level. The principal elements of the conduction band (CB) are the Zr-d, Ir-d, and Co-d states, with the Zr-d states making higher contributions.

It is worth mentioning that within the valence region, all half-Heusler alloys demonstrate overlaps of the Zr-d and Sb-p states, as observed in the density of states (DOS). This observation suggests a strong covalent bonding between the Zr and Sb atoms. Conversely, the contributions from the s orbitals of Co and Ir, as well as the d orbital of Sb, are relatively minor in both the valence and conduction bands.

3.3. Mechanical properties

In the present paper, the mechanical properties of half-Heusler alloys have been examined as important characteristics. The way a material reacts to outside forces and the ensuing deformations is referred to as its mechanical properties. A solid's elastic constants are crucial variables that set requirements for the compound's mechanical stability. They can also provide information about a material's strength, brittleness or ductility, hardness, sound velocity, Young's modulus, Poisson's ratio, shear modulus, bulk modulus, and anisotropy factor. Understanding these properties is crucial to selecting the right materials for different technical applications. The IRelast package, developed by Jamal Morteza [65] and implemented within the WIEN-2K package, was used to calculate the elastic properties of these alloys.

The elastic constants consist mostly of 81 independent components and are a fourth-rank tensor. Nevertheless, this number is lowered by accounting for the crystal's symmetry. We have computed three different elastic constants C_{11}, C_{12} and C_{44} for these concentrations of $ZrCo_{1-x}Ir_xSb$ ($x = 0$, 0.25, 0.75, and 1). This is because these alloys exhibit cubic symmetry. The following equation [66] provides the mechanical stability requirements for cubic crystals:

$$C_{11} \succ 0, C_{44} \succ 0, C_{11} - C_{12} \succ 0, C_{11} + 2C_{12} \succ 0 \tag{2}$$

From calculated C_{ij} results, we have determined the elastic anisotropic factor (A), bulk (B), shear (G), Young's (E) modulus of elasticity, and Poisson ratio (ν) in three forms (Voigt, Reuss, and Hill) as follows:

$$A = \frac{2C_{44}}{C_{11} - C_{12}} \tag{3}$$

Voigt's formulas are given as follows:

$$B_V = \frac{C_{11} + 2C_{12}}{3} \tag{4}$$

$$G_V = \frac{C_{11} - C_{12} + 3C_{44}}{5} \tag{5}$$

For the Reuss procedure, the equivalent formulations are

$$B_R = \frac{C_{11} + 2C_{12}}{3} \tag{6}$$

$$G_R = \frac{5C_{44}(C_{11} - C_{12})}{4C_{44} + 3(C_{11} - C_{12})} \tag{7}$$

The bulk and shear moduli that are Hill-averaged can be found from

$$B_H = \frac{B_R + B_V}{2} \tag{8}$$

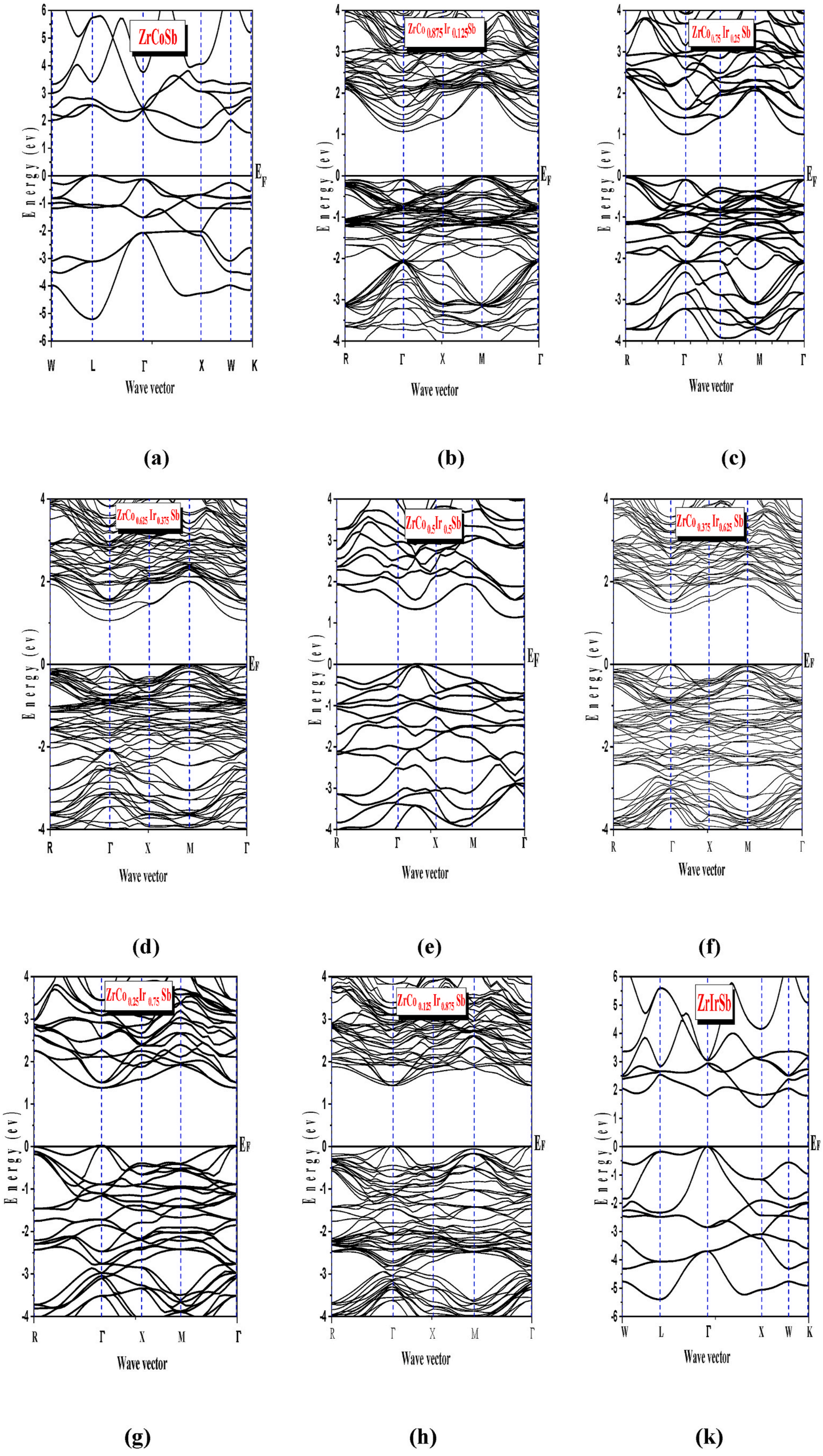

(a) (b) (c)

(d) (e) (f)

(g) (h) (k)

Fig. 8. The band structure of $ZrCo_{1-x}Ir_xSb$ (x = 0, 0.125, 0.25, 0.375, 0.5, 0.625, 0.75, 0.875 and 1) half-Heusler alloys using EV-GGA approximation (a) x = 0, (b) x = 0.125, (c) x = 0.25, (d) x = 0.375, (e) x = 0.5, (f) x = 0.625, (g) x = 0.75, (h) x = 0.875 and (k) x = 1.

Table 5
Calculated band gap E_g (eV) of $ZrCo_{1-x}Ir_xSb$ half-Heusler alloys for various x compositions.

Half-Heusler alloys	*E_g (eV)*				*Other calculations*
	GGA	LDA	mBJ-GGA	EV-GGA	
ZrCoSb	1089	1.118	1.131	1.219	1.06 [61]
$ZrCo_{0.875}Ir_{0.125}Sb$	0,968	0.963	1.017	1.085	
$ZrCo_{0.75}Ir_{0.25}Sb$	0,902	0.920	0.95	1.021	
$ZrCo_{0.625}Ir_{0.375}Sb$	0,949	0.962	1.001	1.073	
$ZrCo_{0.5}Ir_{0.5}Sb$	1002	0.918	1.094	1.164	
$ZrCo_{0.375}Ir_{0.625}Sb$	1112	1.139	1.145	1.248	
$ZrCo_{0.25}Ir_{0.75}Sb$	1257	1.294	1.3	1.401	
$ZrCo_{0.125}Ir_{0.875}Sb$	1,35	1.410	1.404	1.451	
ZrIrSb	1,45	1.471	1.326	1.453	1.40 [61] 1.41 [63]

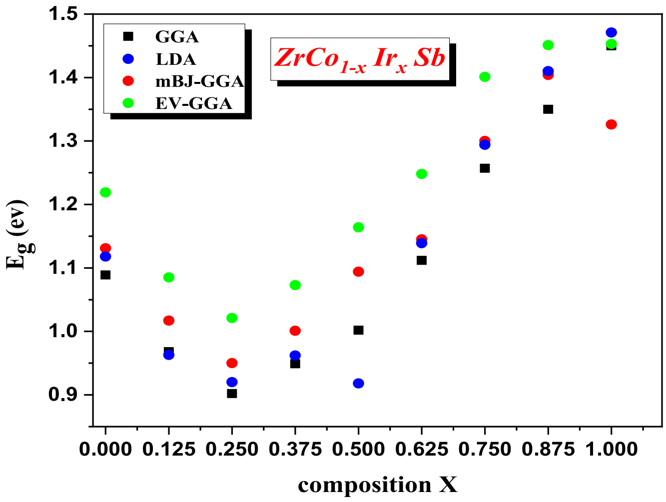

Fig. 9. The band gap E_g (eV) of $ZrCo_{1-x}Ir_xSb$ half-Heusler alloys for various x compositions calculated using GGA, LDA, EV-GGA and mBJ-GGA.

$$G_H = \frac{G_R + G_V}{2} \tag{9}$$

The Young modulus (E) and Poisson ratio (ν) for all averaged processes shown here can be calculated in relation to the bulk modulus (B) and the shear modulus (G) as

$$E = \frac{9BG}{3B + G} \tag{10}$$

$$\nu = \frac{3B - 2G}{2(3B + G)} \tag{11}$$

For these concentrations of $ZrCo_{1-x}Ir_xSb$ (x = 0.125, 0.375, 0.5, 0.625, and 0.875), we have additionally calculated six different elastic constants, C_{11}, C_{33}, C_{44}, C_{66}, C_{12}, and C_{13}, because they exhibit tetragonal symmetry. The following criteria are met by the elastic constants for the mechanically stable tetragonal crystal [67].

$$\begin{aligned} & C_{ii} \succ 0 \quad (i = 1, 3, 4, 6) \\ & C_{11} - C_{12} \succ 0 \\ & C_{11} + C_{33} - 2C_{13} \succ 0 \\ & 2C_{11} + C_{33} + 2C_{12} + 4C_{13} \succ 0 \end{aligned} \tag{12}$$

The single crystal elastic constants C_{ij} and the isotropic bulk moduli B_V and shear moduli G_V of a polycrystalline aggregate have a straightforward relationship, according to the Voigt approximation [68]:

$$B_V = \frac{1}{9}[2(C_{11} + C_{12}) + C_{33} + 4C_{13}] \tag{13}$$

$$G_V = \frac{1}{30}[4C_{11} - 2C_{12} + 12C_{44} + 6C_{66} + 2C_{33} - 4C_{13}] \tag{14}$$

A linear relationship among the isotropic bulk B_R and shear moduli G_R of a polycrystalline aggregate was established by Reuss [69] and is described as follows:

$$B_R = \frac{C^2}{(C_{11} + C_{12}) + 2C_{33} - 4C_{13}} \tag{15}$$

$$G_R = 15 / \left((18B_V) / C^2 + 6 / (C_{11} - C_{12}) + 6 / C_{44} + 3 / C_{66}\right) \tag{16}$$

$$C^2 = (C_{11} + C_{12})C_{33} - 2C_{13}^2 \tag{17}$$

The Hill approximation [70] was used to obtain the equations for B_H, G_H, Young modulus (E) and Poisson ratio (ν) for these $ZrCo_{1-x}Ir_xSb$ (x = 0.125, 0.375, 0.5, 0.625, and 0.875) alloys. These equations are identical to those in expressions (8), (9), (10), and (11), respectively.

A key component in the domains of materials science and material engineering is the hardness of the material. It describes a material's capacity to withstand localized plastic deformation. The hardness expression is given as follows [71]:

$$H = \frac{(1 - 2\nu)E}{6(1 + \nu)} \tag{18}$$

The determined elastic constants for $ZrCo_{1-x}Ir_xSb$ alloys meet the mechanical stability requirements, as indicated in Table 6.

For the studied $ZrCo_{1-x}Ir_xSb$ (x = 0,0.25,0.75 and 1) alloys having cubic structures, the results that follow can be drawn based on the data acquired and presented in Table 6: (*i*) The resistance to unidirectional compression along the a-axis, shown by C_{11}, is significantly greater than the resistance to shear deformation, represented by C_{44}. This suggests that these alloys under study are more resistant to unidirectional compression than shear deformation. (*ii*) Shape elasticity is also characterized by C_{12}. A transverse strain results in a shape change with a constant volume. We found that as the concentration of Ir atoms in the $ZrCo_{1-x}Ir_xSb$ increases, the values of C_{12} and C_{13} rise as well. Regarding alloys that possess tetragonal structures, the resistances to linear compression in the x and z directions are indicated by the elastic constants C_{11} and C_{33}, respectively, as is widely known, but the elasticity in form is connected to the elastic constants C_{12}, C_{13}, C_{44}, and C_{66} accordance with Table 6. At concentrations of $ZrCo_{1-x}Ir_xSb$ (x = 0.375 and x = 0.5), the value of C_{33} is greater than C_{11}. Accordingly, $ZrCo_{0.625}Ir_{0.375}Sb$ and $ZrCo_{0.5}Ir_{0.5}Sb$ alloys ought to compress more readily along the x-axis than the z-axis [72], and for $ZrCo_{1-x}Ir_xSb$ (x = 0.125 and x = 0.875) concentrations, C_{11} is greater than C_{33}. Consequently, $ZrCo_{0.875}Ir_{0.125}Sb$ and $ZrCo_{0.125}Ir_{0.875}Sb$ alloys should compress more readily along the z-axis than the x-axis. Furthermore, the fact that C_{66} is less than C_{44} suggests that the [1 0 0] in the plane (0 1 0) shear is simpler than the [1 0 0] in the plane (0 0 1) shear for these alloys, with the exception of the $ZrCo_{0.5}Ir_{0.5}Sb$ alloy [73].

Table 7 provides an overview of the mechanical properties results we obtained. The bulk moduli calculated and derived using elastic constants closely match those obtained from Murnaghan's equation of state. This resemblance could be used to gauge how accurate and dependable this theoretical calculation of the elastic constants is. Based on Table 7, the computed bulk moduli for ZrIrSb (B_H = 149.237 GPa) have a higher value than for other alloys, indicating that ZrIrSb has a higher elastic stiffness than the other alloys. With G_H values ranging from 68.014 GPa to 85.404 GPa and modest proximity to one another, these $ZrCo_{1-x}Ir_xSb$ half-Heusler alloys exhibit strong atomic bonding and a high shear modulus.

The stiffness of an elastic material is expressed in terms of its Young's modulus. A high Young's modulus indicates that the material is stiff. In this case, the material ZrCoSb has the highest Young's modulus, which is a measure of stiffness, with a value of 205.502 GPa. On the other hand,

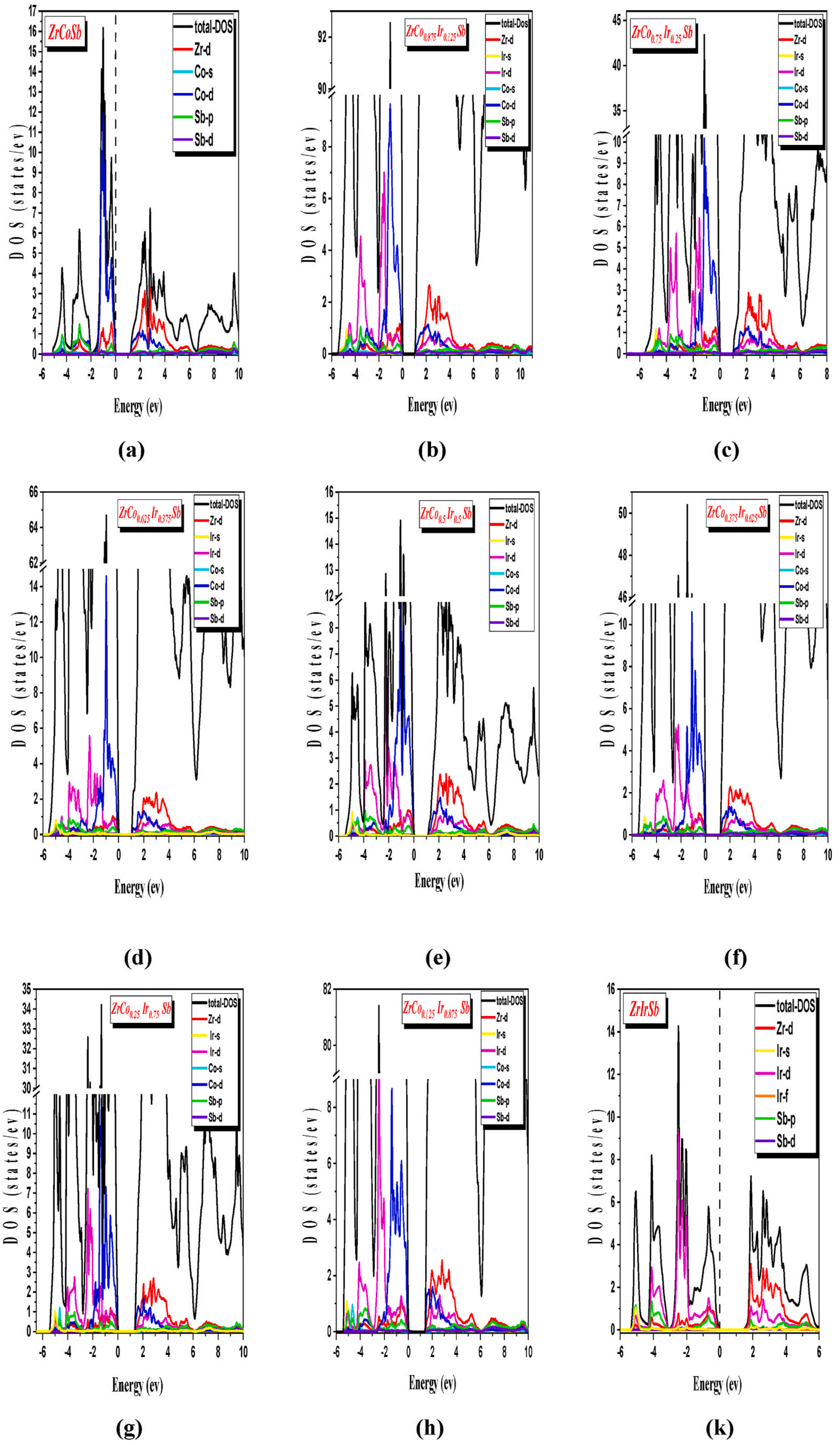

Fig. 10. The total and partial density of states of $ZrCo_{1-x}Ir_xSb$ (x = 0, 0.125, 0.25, 0.375, 0.5, 0.625, 0.75, 0.875 and 1) half-Heusler alloys using EV-GGA approximation (a) x = 0, (b) x = 0.125, (c) x = 0.25, (d) x = 0.375, (e) x = 0.5, (f) x = 0.625, (g) x = 0.75, (h) x = 0.875 and (k) x = 1.

Table 6

The elastic constants in GPa for HH alloys $ZrCo_{1-x}Ir_xSb$ (x = 0, 0.125, 0.25, 0.375, 0.5, 0.625, 0.75, 0.875 and 1) were computed using GGA approximation.

The compounds	*Elastic Constants*					
	C_{11}	C_{33}	C_{44}	C_{66}	C_{12}	C_{13}
ZrCoSb	245.1871	–	78.2476	–	50.4579	-
$ZrCo_{0.875}Ir_{0.125}Sb$	252.3565	251.7928	73.3990	71.8659	71.4320	71.1438
$ZrCo_{0.75}Ir_{0.25}Sb$	249.1501	–	79.0863	–	80.0736	-
$ZrCo_{0.625}Ir_{0.375}Sb$	237.3663	237.6766	76.4952	74.0309	79.3299	78.9653
$ZrCo_{0.5}Ir_{0.5}Sb$	227.2118	236.8892	67.2495	73.3566	87.6786	82.6070
$ZrCo_{0.375}Ir_{0.625}Sb$	235.4416	235.6130	84.7316	82.4938	91.6169	91.3555
$ZrCo_{0.25}Ir_{0.75}Sb$	236.7720	–	84.1423	–	94.9882	–
$ZrCo_{0.125}Ir_{0.875}Sb$	229.4876	228.9239	69.8895	67.6656	98.5518	95.57
ZrIrSb	235.7977	–	91.0978	–	105.9587	–

Table 7

Modules of elasticity in GPa B_V, B_R, B_H, G_V, G_R, G_H, E_V, E_R, E_H, ν_V, ν_R, ν_H and Hardness H for HH alloys $ZrCo_{1-x}Ir_xSb$ (x = 0, 0.125, 0.25, 0.375, 0.5, 0.625, 0.75, 0.875 and 1) were using GGA approximation.

Elasticity Modules	*The composition* x								
	x = 0	x = 0.125	x = 0.25	x = 0.375	x = 0.5	x = 0.625	x = 0.75	x = 0.875	x = 1
B_V	115.367	131.549	136.432	131.881	133.01	139.461	142.249	140.809	149.238
B_R	115.367	131.549	136.432	131.881	133	139.461	142.249	140.802	149.237
B_H	115.367	131.549	136.432	131.881	133.005	139.461	142.249	140.805	149.237
G_V	85.893	79.917	81.266	77.08	70.799	79.202	78.841	68.035	80.625
G_R	84.916	79.024	81.18	77.031	70.621	78.748	78.289	67.993	78.444
G_H	85.404	79.47	81.223	77.055	70.71	78.975	78.565	68.014	79.534
E_V	206.444	199.376	203.41	193.535	180.39	199.785	199.639	175.792	204.964
E_R	204.559	197.52	203.231	193.432	180.003	198.821	198.458	175.697	200.246
E_H	205.502	198.448	203.32	193.482	180.197	199.303	199.049	175.744	202.609
ν_V	0.201	0.247	0.251	0.255	0.273	0.261	0.266	0.291	0.271
ν_R	0.204	0.249	0.251	0.255	0.273	0.261	0.267	0.292	0.271
ν_H	0.203	0.248	0.251	0.255	0.274	0.261	0.266	0.291	0.273
H	16.91	13.35	13.48	12.59	10.65	12.59	12.26	9.48	12.04

Table 8

The calculated shear anisotropic factors (A, A_1, A_2 and A_3) for HH alloys $ZrCo_{1-x}Ir_xSb$ (x = 0, 0.125, 0.25, 0.375, 0.5, 0.625, 0.75, 0.875 and 1).

The compounds	A	A_1	A_2	A_3
ZrCoSb	0.80366	–	–	–
$ZrCo_{0.875}Ir_{0.125}Sb$	–	0.81135	0.8566	0.79443
$ZrCo_{0.75}Ir_{0.25}Sb$	0.93551	–	–	–
$ZrCo_{0.625}Ir_{0.375}Sb$	-	0.9649	0.98046	0.93688
$ZrCo_{0.5}Ir_{0.5}Sb$	–	0.9	0.88949	1.05146
$ZrCo_{0.375}Ir_{0.625}Sb$	-	1.17543	1.13444	1.14714
$ZrCo_{0.25}Ir_{0.75}Sb$	1.18691	–	–	–
$ZrCo_{0.125}Ir_{0.875}Sb$	-	1.04597	1.03748	1.03357
ZrIrSb	1.40324	–	–	–

the material $ZrCo_{0.125}Ir_{0.875}Sb$ has the lowest Young's modulus, indicating the least stiffness, with a value of 175.744 GPa. Among these alloys, ZrCoSb has the comparatively greatest Young's and shear moduli, indicating high hardness and powerful bonding. A solid's Poisson's ratio value for stable alloys is 1 to 0.5 [74]. Table 7 demonstrates that the HH alloys' Poisson's ratio values range from 0.203 to 0.291, indicating that these alloys are stable under shear stress.

According to Table 7, the ZrCoSb half heusler has the highest measured hardness compared to other HH alloys with a value of 16.91 GPa. All of our HH alloys are also classified as hard materials because their hardness values are all equal to or higher than 9 GPa.

Due to its correlation with the potential to generate microcracks in materials, elastic anisotropy, which represents varying bonding natures in various crystallographic directions, has significant implications [72]. An accurate characterization of anisotropic behavior has significant implications for solid-state science and engineering research. Along the (100), $(1\overline{1}0)$, and (001) shear planes, the shear anisotropic factors have been defined in the following order [73]:

$$A_1 = \frac{4C_{44}}{C_{11} + C_{33} - 2C_{13}} \tag{19}$$

$$A_2 = \frac{C_{44}(C_L + 2C_{13} + C_{33})}{(C_L C_{33} - C_{13}^2)} \tag{20}$$

$$A_3 = \frac{2C_{66}}{C_{11} - C_{12}} \tag{21}$$

With $C_L = C_{66} + (C_{11} + C_{12})/2$.

Table 8 presents a list of the obtained anisotropic factors. Four anisotropic factors have been estimated in this instance: A for cubic crystals and A_1, A_2 and A_3 for tetragonal crystals, The values of A, A_1, A_2 and A_3 for an isotropic crystal equal 1, and a value less or greater than 1 indicates the degree of shear anisotropy the crystal possesses [75]. Shear anisotropy appears to be greater in the (100) and $(1\overline{1}0)$ shear planes for alloys with tetragonal crystals. The ZrIrSb cubic crystal exhibits the greatest value (A = 1.40324), which demonstrates that, in comparison to the other alloys, this one has good isotropy. Additionally, it is noted that as the Ir atom's concentration in $ZrCo_{1-x}Ir_xSb$ increases, the values of A rise.

To fully describe the mechanical properties of ZrCo1-xIrxSb, we calculated Debye temperature θ_D, a fundamental parameter that is closely linked to numerous physical properties of solids, like elastic constants, specific heat, and melting temperature, from isotropic longitudinal, transverse, and average sound wave velocities (V_l, V_t, and V_m) using the equations that follow [76–78]:

$$\theta_D = \frac{h}{k_B} V_m \left(\frac{3n}{4\pi} \frac{N_A \rho}{M} \right)^{1/3} \tag{22}$$

$$V_l = [(3B + 4G)/3\rho]^{1/2} \tag{23}$$

Table 9
transversal, Longitudinal and average sound velocity ($V_t V_l$, V_m in m/s), Debye temperature (θ_D in K) for HH alloys $ZrCo_{1-x}Ir_xSb$ (x = 0, 0.125, 0.25, 0.375, 0.5, 0.625, 0.75, 0.875 and 1) were using GGA approximation.

The compounds	$V_t(m/s)$	$V_l(m/s)$	$V_m(m/s)$	$\theta_D(K)$
ZrCoSb	3279.97	5373.72	3622.24	404.432
$ZrCo_{0.875}Ir_{0.125}Sb$	3098.59	5356.76	3439.45	381.763
$ZrCo_{0.75}Ir_{0.25}Sb$	3074.91	5337.48	3414.39	376.592
$ZrCo_{0.625}Ir_{0.375}Sb$	2946.35	5141.24	3273.12	358.564
$ZrCo_{0.5}Ir_{0.5}Sb$	2773.68	4972.8	3088.22	336.553
$ZrCo_{0.375}Ir_{0.625}Sb$	2882.97	5075.36	3205.12	347.575
$ZrCo_{0.25}Ir_{0.75}Sb$	2824.03	5007.31	3141.45	339.569
$ZrCo_{0.125}Ir_{0.875}Sb$	2591.23	4780.5	2891.42	310.882
ZrIrSb	2759.59	4944	3072.36	329.081

$$V_t = (G/\rho)^{1/2} \tag{24}$$

$$V_m = \left[\frac{1}{3}\left(2V_t^{-3} + V_l^{-3}\right)\right]^{-1/3} \tag{25}$$

Where the symbols h, k_B, ρ, N_A, M, n, B and G correspondingly signify Planck's constant, Boltzman's constant, mass density, Avogadro number, molecular weight, number of atoms in the molecule, bulk modulus and shear modulus. Table 9 shows the computed values for Debye temperature (θ_D) and sound velocities (V_l, V_t, and V_m) at zero pressure.

The computed values of Debye temperature, the longitudinal, transverse and average sound velocities appear in Table 9. In this instance, ZrCoSb has the highest Debye temperature (404.432 K) among the alloys. This ZrCoSb value suggests stronger chemical bonding and comparatively superior thermal conductivity in the crystal structure. Table 9 further demonstrates that all HH alloys have longitudinal sound velocities that are significantly faster than transverse velocities.

4. Conclusions

We studied the structural and electronic properties of $ZrCo_{1-x}Ir_xSb$ half-Heusler alloys at different concentrations (x = 0, 0.125, 0.25, 0.375, 0.5, 0.625, 0.75, 0.875 and 1) with cubic structures by emeploying the full-potential linearized-augmented plane wave method (FP-LAPW). GGA, LDA, EV-GGA, and mBJ-GGA approximations were used to handle the exchange-correlation potential. According to the structural properties, the (4b, 4c, 4a) arrangement structure is the most stable for the ternary alloys. We also observed its nonmagnetic state, and it is observed that the estimated lattice constant and bulk modulus rise with a concentration increase of the Ir atom in $ZrCo_{1-x}Ir_xSb$, where the lattice parameters for ternary compounds accord reasonably well with theoretical values. As to the electronic band structure calculation, all compounds are indirect semiconductors, except for $ZrCo_{0.25}Ir_{0.75}Sb$ and $ZrCo_{0.125}Ir_{0.875}Sb$, which have a direct band gap. In contrast, substituting Ir for Co causes significant changes in the electronic structures of the ternary alloys ZrCoSb and ZrIrSb. In Co compounds, the valence band maximum happens at the L point, but in Ir compounds, it happens at the Γ point. Furthermore, the band gap shows nonlinear behavior in relation to the composition x. When compared to previous theoretical results, the result achieved with EV-GGA potential is superior to that produced with mBJ-GGA potential. Additionally, we computed the mechanical properties of these alloys and found that $ZrCo_{1-x}Ir_xSb$ exhibits stable elastic behavior. We discussed the elastic constants, bulk modulus, shear modulus, Young's modulus, Poisson's ratio, hardness, shear anisotropy factor, sound velocities and Debye temperature. It was observed that there is an upward correlation between the concentration of Ir atoms in $ZrCo_{1-x}Ir_xSb$ and the values of C_{12}, C_{13} and shear anisotropic factors. Since every one of our HH alloys has a hardness rating of at least 9 GPa, they are all categorized as hard materials as well. The future experimental investigation may be motivated by the description of the electronic, structural and mechanical properties of $ZrCo_{1-x}Ir_xSb$ (x = 0, 0.125, 0.25, 0.375, 0.5, 0.625, 0.75, 0.875 and 1) compounds.

CRediT authorship contribution statement

B. Abdelkebir: Conceptualization, Formal analysis, Investigation, Writing – original draft. **Z. Charifi:** Formal analysis, Methodology, Supervision, Writing – original draft, Writing – review & editing. **H. Baaziz:** Data curation, Investigation, Software, Validation, Writing – review & editing. **T. Ghellab:** Conceptualization, Investigation, Methodology, Software. **R. Khenata:** Conceptualization, Data curation, Supervision, Writing – review & editing. **S. Bin-Omran:** Conceptualization, Data curation, Software.

Declaration of competing interest

I declare that we have no known competing financial interests or personal relationships that could have appeared to influence the work reported in this paper.

Data availability

Data will be made available on request.

Acknowledgments

The authors (H. Baaziz,T. Ghellab and Z. Charifi) would like to express gratitude to the General Directorate for Scientific Research and Technological Development for the financial assistance they provided over the course of this work's execution. The author Bin-Omran acknowledges Researchers Supporting Project number (RSP-2024R82), King Saud University, Riyadh, Saudi Arabia.

References

[1] M. Ziese and M. J. Thornton (ed) Spin Electronics (Berlin : Springer).
[2] G.A. Prinz, Science 282 (2001) 1660.
[3] H. Munekata, H. Ohno, S. von Molnar, A. Segmoller, L.L. u Chang, L. Esaki, Phys. Rev. Lett. 63 (1989) 1849.
[4] H.C. Torrey, Phys. Rev. B 104 (1956) 563.
[5] P.M. Levy, Solid State Phys. 47 (1994) 367.
[6] P. Gronberg, R. Schreiber, Y. Pang, M.D. Brodsky, H. Sowers, Phys. Rev. Lett. 57 (1986) 2442.
[7] N.F. Mott, Proc. Phys. Soc. 47 (1935) 571.
[8] J.Q. Xiao, J.S. Jiang, C.L. Chien, Phys. Rev. Lett. 68 (1992) 3749.
[9] R.J. Jr. Soulen, et al., Science 282 (1998) 85.
[10] A. Hirohat, K. Takanashi, Phys. Rev. 980–8577 (2014).
[11] S.K. Upadhyay, R.N. Louie, R.A. Buhrman, Appl. Phys. Lett. 74 (1991) 3881.
[12] W.H. Rippard, R.A. Buhrman, Phys. Rev. Lett. 84 (2000) 971.
[13] Johnson, Amsterdam, J.S. Moodera, R.H. Meservey, Spinpolarized Tunnelling Magnetoelectronics, 2004.
[14] M.N. Baibich, J.M. Broto, A. Fert, F.N. Van Dau, F. Petroff, P. Etienne, G. Creuzet, A. Friederich, J. Chazelas, Phys. Rev. Lett. 61 (1988) 2472.
[15] U. Hartmann (ed) Magnetic Multilayers and Giant Magnetoresistance (Berlin : Springer)(2000).
[16] A. Yamaguchi, T Ono, S. Nasu, K. Miyake, K. Mibu and T. Shinjo, Phys. Rev. Lett. 92 (2004)077205.
[17] M. Julliére, Phys. Lett. 54 (1975) 225.
[18] C. Chappert, A. Fert, F.N. van Dau, Nat. Mater. 6 (2007) 813–823.
[19] P.J. Webster, K.R.A. Ziebeck, Alloys and Compounds of D-Elements with Main Group Elements, Springer, Berlin, 1988.
[20] K.R.A. Ziebeck, K.U. Neumann, Magnetic Properties of Metals, Springer, Berlin, 2001.
[21] C.M. Fang, G.A. de Wijs, R.A. de Groot, J. Appl. Phys. 91 (2002) 8340.
[22] S.A. Wolf, D.D. Awschalom, R.A. Buhrman, J.M. Daughton, S. Von Molnar, M. L. Roukes, A.Y. Chtchelkanova, D.M. Treger, Science 294 (2001) 1488.
[23] W. Jeitschko, Metall. Trans. A 1 (1970) 3159.
[24] N. Mott, Adv. Phys. 13 (1964) 325.
[25] R.W.G. Wyckoff, Crystal Structures, second ed., John Wiley & Sons, United States, 1963.
[26] C. Felser, B. Hillebrands, J. Phys. D Appl. Phys. 42 (2009) 080301.
[27] Z. Deng, et al., Nat. Commun. 2 (2011) 422.
[28] M. Ahmad, G. Murtaza, R. Khenata, S.B. Omran, A. Bouhemadou, et al., J. Magn. Magn Mater. 377 (2015) 204–210.
[29] Y. Xia, V. Ponnambalam, S. Bhattacharya, A.L. Pope, S.J. Poon, T.M. Tritt, J. Phys. Condens. Matter 13 (1) (2001) 77.
[30] B. Alling, S. Shallcross, I.A. Abrikosov, Phys. Rev. B 73 (2006) 064418.

[31] H. Mehnane, et al., Superlattices and Microstructures 51.6, 2012 ,, pp. 772–784.

[32] Frederick Casper, Ram Seshadri, Claudia Felser, Phys. Status Solidi 206 (5) (2009) 1090–1095. .

[33] S. Kacimi, H. Mehnane, A. Zaoui, J. Alloys Compd. 587 (2014) 451–458. .

[34] Fleur Legrain, et al., J. Phys. Chem. B 122 (2) (2018) 625–632. .

[35] David Kieven, et al., Phys. Rev. B 81 (7) (2010) 075208. .

[36] D. Jung, H.-J. Koo, M.-H. Whangbo, J. Mol. Struct.: THEOCHEM 527 (2000) 113–119. .

[37] Maedeh Zahedifar, Peter Kratzer, Phys. Rev. B 97 (2018) 035204. .

[38] D.F. Zou, et al., J. Appl. Phys. 113 (2013) 193705. .

[39] Abhinav Nag, Yuhit Gupta, Jagdish Kumar, Mater. Chem. Phys. 297 (2023) 127373. .

[40] Kalita Dipangkar, Yuhit Gupta, Atul Saxena, Bull. Mater. Sci. 45 (2022) 144..

[41] S. Chibani, et al., J. Electron. Mater. 47 (2018) 196–204. .

[42] Yuhit Gupta, M.M. Sinha, S.S. Verma, Phys. B Condens. Matter 624 (2022) 413425. .

[43] Yuhit Gupta, M.M. Sinha, S.S. Verma, Mater. Today Commun. 27 (2021) 102195. .

[44] Yuhit Gupta, M.M. Sinha, S.S. Verma, Mater. Chem. Phys. 265 (2021) 124518. .

[45] Yuhit Gupta, M.M. Sinha, S.S. Verma, Mater. Today Commun. 26 (2021) 101885. .

[46] W. Kohn, L.J. Sham, Phys. Rev. 140 (1965) A1133–A1138.

[47] P. Hohenberg, W. Kohn, Phys. Rev. 136 (1964) B864.

[48] O.K. Andersen, Phys. Rev. B 12 (1975) 3060–3083.

[49] Elisabeth Sjöstedt, Lars Nordström, D.J. Singh, Solid State Commun. 114 (2000) 15–20. .

[50] P. Blaha, K. Schwarz, G.K.H. Madsen, D. Kvasnicka, J. Luitz, WIEN 2K, an augmented plane wave + local orbitals program for calculating crystal properties, in: K. Schwarz (Ed.), Techn. Universität, 2001. Wien.

[51] J.C. Slater, Phys. Rev. 51 (1937) 846–851.

[52] J.P. Perdew, Zunger, Phys. Rev. B 23 (1981) 5048.

[53] J.P. Perdew, K. Burke, M. Ernzerhof, Phys. Rev. Lett. 77 (1996) 3865.

[54] E. Engel, S.H. Vosko, Phys. Rev. B47 (1993) 20.

[55] F. Tran, P. Blaha, Phys. Rev. Lett. 102 (2009) 226401.

[56] Francis Dominic Murnaghan, Proc. Natl. Acad. Sci. USA 30 (1944) 244–247. .

[57] Francis Birch, Phys. Rev. 71 (1947) 809. .

[58] L. Vegard, Z. Phys. 5 (1921) 17.

[59] Sekimoto Takeyuki, et al., "Thermoelectric and thermophysical properties of TiCoSb, ZrCoSb, HfCoSb prepared by SPS." ICT 2005, in: 24th International Conference on Thermoelectrics, 2005, IEEE, 2005.

[60] C.B.H. Evers, C.G. Richter, K. Hartjes, W. Jeitschko, J. Alloys Compd. 252 (1997) 93.

[61] Mal-Soon Lee, Ferdinand P. Poudeu, S.D. Mahanti, Phys. Rev. B 83 (2011) 085204. .

[62] Minping Zhang, Junhong Wei, Guangtao Wang, Phys. Lett. 382 (9) (2018) 673–678. .

[63] Kavita Yadav, et al., J. Phys. D Appl. Phys. 54 (2021) 495303. .

[64] S. Ogut, K.M. Rabe, Phys. Rev. B 51 (1995) 10443.

[65] Morteza Jamal, et al., IRelast package, J. Alloys Compd. 735 (2018) 569579. .

[66] Zhi-jian Wu, et al., Phys. Rev. B 76 (2007) 054115. .

[67] Max Born, On the stability of crystal lattices. I, Math. Proc. Camb. Phil. Soc. 36 (2) (1940). Cambridge University Press.

[68] W. Voigt, Lehrbuch der Kristallphysik, Taubner, Leipzig, 1928.

[69] A. Reuss, Z. Angew, Math. Mech. 9 (1929) 5566.

[70] R. Hill, Proc. Soc. London A 65 (1952) 350362.

[71] G. Rogl, et al., Acta Mater. 107 (2016) 178–195.

[72] N. Guechi, et al., Solid State Sci. 29 (2014) 12–23. .

[73] Meng-Xue Zeng, et al., Model. Simulat. Mater. Sci. Eng. 20 (2012) 035018. .

[74] Longke Bao, et al., Solid State Sci. 98 (2019) 106027. .

[75] Naihua Miao, et al., Theoretical investigation on the transition-metal borides with Ta3B4-type structure: a class of hard and refractory materials, Comput. Mater. Sci. 50 (4) (2011) 1559–1566. .

[76] P. Ravindran, et al., Density functional theory for calculation of elastic properties of orthorhombic crystals: application to TiSi 2, J. Appl. Phys. 84 (9) (1998) 4891–4904.

[77] Orson L. Anderson, A simplified method for calculating the Debye temperature from elastic constants, J. Phys. Chem. Solid. 24 (7) (1963) 909–917. .

[78] Edward Schreiber, et al., Elastic Constants and Their Measurement, 1975 ,, pp. 747–748.